Heliyon 9 (2023) e17191

Contents lists available at ScienceDirect

Heliyon

journal homepage: www.cell.com/heliyon

Research article

Effects of activation overpotential in photoelectrochemical cells considering electrical and optical configurations

Abdul Ahad Mamun, Asif Billah, Muhammad Anisuzzaman Talukder *

Department of Electrical and Electronic Engineering, Bangladesh University of Engineering and Technology, Dhaka 1205, Bangladesh

A B S T R A C T

Photoelectrochemical cells (PECs) are a promising option for directly converting solar energy into chemical energy by producing hydrogen (H_2) gas, thus providing a clean alternative to consuming fossil fuels. H_2 as fuel is free from any carbon footprints and negative environmental impacts. Therefore, the H_2 production, especially directly using sunlight in PECs, is critically important for the rapidly growing energy demand of the world. Although promising, PECs are inefficient and must overcome a few inherent losses in producing H_2—the most important being the activation overpotential (η_a) required for splitting water. This work analyzes the impact of η_a on solar-to-fuel efficiency (η_{STF}) and H_2 production rate (HPR). This work also discusses choosing appropriate photo-absorbing materials based on their energy bandgaps and suitable electrode pairs to achieve desired η_{STF} and HPR for different electrical and optical PEC configurations. Significant changes are observed in η_{STF} and HPR when η_a is considered in water splitting.

1. Introduction

Photoelectrochemical cells (PECs) produce hydrogen (H_2) gas by splitting water using solar energy and suitable photo-absorbing semiconductors [1–4]. In PECs, light energy dissociates water molecules into H_2 and oxygen (O_2) [5,6]. Conventional energy sources, such as fossil fuels, are limited. Fossil fuels cause irreparable environmental damage by producing greenhouse gases, such as carbon dioxide (CO_2). Therefore, reducing CO_2 emissions is the most urgent need of time to save the earth's climate. In addition, fossil fuels will not last long and are estimated to be depleted by 2100 if burning continues at the present rate [7]. In the recent UN climate change conference (COP26) in Glasgow, world leaders proposed to reduce the carbon footprint rate to zero by the year 2050 [8]. Therefore, fossil fuel dependency needs to be reduced, and alternative solutions must replace fossil fuels in applications soon. The best alternative energy solutions lie with renewable sources. Among the renewable energy sources, solar energy is drawing significantly more attention [9–12]. Solar energy can be converted into chemical energy by splitting water and producing H_2 gas. Renewable solar H_2 gas is a clean and green alternative to fossil fuels, especially for its applications in the automotive sector. When burned in fuel cells, H_2 produces only water [13–16].

The initial reports on electrochemical photolysis drew attention to finding new anode and cathode materials for water splitting [17–24]. Initial research initiatives also aimed to increase the obtainable voltage and current by exploring different optical and electrical configurations [25]. Significant research has also been conducted to obtain appropriate anode and cathode materials in PECs [2,5,26–30]. Several mixed transition metal oxides have been used in the last two decades for efficient photoelectrochemical H_2 production [4]. Due to their exceptional photoelectrochemical stability, low cost, suitable band-edge locations, and widespread bandgap dispersion, metal oxides have drawn much attention. Significant advancements in creating metal oxide nanoparticles for PEC water splitting have been made during these decades. To name a few, TiO_2, ZnO, WO_3, and Fe_2O_3 have been thoroughly investigated

* Corresponding author.
E-mail address: anis@eee.buet.ac.bd (M. Anisuzzaman Talukder).

https://doi.org/10.1016/j.heliyon.2023.e17191
Received 19 February 2023; Received in revised form 7 June 2023; Accepted 9 June 2023

Available online 15 June 2023

for PEC water splitting [31]. Recently, semiconductor and carbon quantum dots (QDs) have been increasingly used due to their suitable shapes, sizes, compositions, tunable absorption spectrum, ease of surface functionalization, and outstanding electron transfer efficiency [32–34]. Their large surface area relative to their volume improves QD's ability to absorb light. In addition to serving as electron reservoirs to support photo-generated electrons with much reduced electron-hole recombination, the newly discovered QDs might also function as photosensitizers to improve solar light harvesting, resulting in significantly improved PEC performance. To date, QD-based photocatalysts, ZnO, Cu_2ZnGeS_4, CuInSSe/ZnS, Zn-$CuInSe_2$/$CuInS_2$, $Cd_xZn_{1-x}S$ have been extensively investigated for photocatalytic applications [34–36].

Although experimental reports of PEC performances are common in literature, a detailed theoretical treatment of this topic is still lacking. In addition, to date, theoretical analyses report solar-to-fuel efficiency (η_{STF}) and H_2 production rate (HPR) considering only ideal PECs, where η_{STF} and HPR are not affected by any losses [37–39]. However, losses are inherent to PECs, and realistic implementations of efficient PECs are impossible without considering the losses incurred [40–43].

The efficiency of an ideal PEC for water splitting will be greater than a PEC working in a practical scenario. In practice, several losses pertinent to the electrodes, electrolyte, and junctions, such as overpotential, shunt losses, resistance losses of the contacts, charge carrier transportation losses, junction losses, thermodynamic and radiative recombination losses, and polarization losses, impact the performance of a PEC. Due to these losses, η_{STF} does not reach the desired level. Among the losses incurred, the overpotential loss within the electrode and the resistance loss within the electrolyte are the primary concerns [13,44–51]. The overpotential is the excess potential applied to an electrode to initiate electron transfer from the electrode to the electrolytic solution in an electrochemical cell. The value of η_{STF}, considering the overpotential loss, can be less than half of that when considering an ideal situation [52]. Also, the selection of electrodes is critical due to the losses [53], and the studies of losses due to electrode materials is a crucial issue. The electrode materials should be selected based on high exchange current density, low overpotentials, strong conductivity, and good stability.

Photo-absorbing materials can be used as electrodes in PECs in addition to absorbing light and generating electric potential [5,54]. In this case, materials must have both photo-absorbing characteristics and those required for water splitting, making it challenging to meet both. For effective light harvesting and electron transfer, photo-absorbing materials should have the following qualities: a bandgap that matches the required potential, a high absorption coefficient, a large surface area to maximize the number of active sites, and stability. For a single photo-absorber, obtaining the required electric potential for water splitting is met only by a single E_g. For double or triple photo-absorber, the standard potential of H^+/H_2 and O_2/H_2O would be achieved by E_gs of all photo-absorbing materials. Therefore, different materials are often used for electrodes and photo-absorbers. In this case, photo-absorbing materials are only used to generate the open-circuit voltage (V_{oc}) and short-circuit current density (J_{sc}) by absorbing the solar irradiance spectrum, as used in this work. Separate electrodes and photo-absorbers offer a negligible loss at the electrode–photo-absorbing material junction, considered an ohmic contact in PEC [55,56].

The structural designs of PECs may vary in optical and electrical configurations. The optical configuration focuses on efficiently harvesting light, and the electrical configuration is for transporting photo-excited charge carriers. Both optical and electrical configurations may be series, parallel, and a combination of series and parallel. The positions of electrodes depend on the branches of an electrical configuration. Different current densities flow through different branches in a mixed electrical configuration. Hence, η_{STF} and overpotential losses (η) also vary depending on the PEC configuration. Furthermore, the positions of electrodes in an electrical configuration cause current density (J) to vary from branch to branch. Therefore, η_a also varies for different PEC configurations. The variation of η_{STF} leads to significant changes in H_2 production.

To date, there are no detailed reports on the effects of η_a on η_{STF} and HPR for H_2 generation. This work investigates how η_a depends on bandgap energy (E_g) and J_{sc} considering different electrode pairs. This work also investigates the effects of η_a on η_{STF} and HPR for different photo-absorbing and electrode materials. Libraries of photo-absorbing and electrode materials have been created. PEC η_{STF} and HPR are analyzed for several combinations of photo-absorbing and electrode materials. The bandgaps of photo-absorbing materials are determined for optimized η_{STF} and HPR for several electrical and optical configurations considering the impact of η_a. Also, this work analyzes the impact of electrode positions in electrical branches and discusses the selection of compatible electrode pairs considering η_a. Due to η_a, choosing compatible photo-absorbers is a difficult task for any PEC configuration as a slight variation of η_a causes a significant change in J. The values of η_{STF} and HPR change significantly when η_a is considered in the calculation. Finally, this work illustrates PEC designs considering the material parameters, electrical and optical configurations, and the number of electrolyzers.

2. Theoretical modeling

At standard conditions, the Gibbs free energy, $\Delta G = 237.2$ kJ/mol, changes when H_2 and $1/2O_2$ are obtained from a H_2O molecule. The change in free energy indicates $\Delta E^0 = 1.23$ eV per electron transferred according to the Nernst equation [5]. Therefore, the photo-absorbing material must absorb photon irradiance with energy > 1.23 eV and convert it into H_2 and O_2. Here, a photon with > 1.23 eV has a wavelength ≤ 1000 nm [57]. However, due to losses in a practical scenario, there is a need for an additional ≳ 0.4–0.6 eV for water splitting [29,52]. A PEC water splitting system must generate two electron-hole pairs per molecule of H_2 or four electron-hole pairs per molecule of O_2.

A single semiconductor material can drive the H_2 (HER) and O_2 evolution reactions (OER) using electrons and holes generated under illumination. The material must have an E_g greater than that required to split water and conduction (E_{cb}) and valence band-edge energies (E_{vb}) that straddle the electrochemical potentials $E^0(H^+/H_2)$ and $E^0(O_2/H_2O)$ [57]. If a single semiconductor material does not meet the required potential for water splitting, multiple semiconductor materials can be used in tandem, providing sufficient

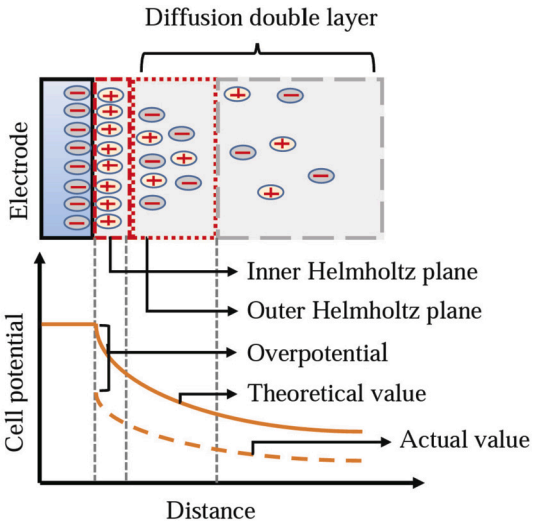

Fig. 1. Schematic illustration of the electric double layer (EDL) with Helmholtz plane between an electrode and electrolytic solution and the corresponding cell potential.

electrochemical potential for HER and OER. Tandem cells are a stack of multiple photo-absorbing materials on top of each other, effectively capturing solar energy. They are classified into two categories: (1) type A tandem cells have two terminals, one connected to the top of the cell and the other to the bottom, and (2) type B tandem cells have multiple terminals, separate connections with each photo-absorber. Band alignment is not a problem for type B cells. However, band alignment is crucial for type A cells for which the conduction band of the photo-absorbing material at the anode side is more negative than the valence band at the cathode side, and the band gap of the photo-absorber should be sufficient for H^+/H_2 or O_2/H_2O standard potential for HER and OER [58]. The HER and OER can be written as

$$H_2O \rightarrow \frac{1}{2}O_2 + H_2 \qquad \Delta G = +237.2 \qquad \text{kJ/mol}, \tag{1a}$$

$$2H^+ + 2e^- \rightarrow H_2 \qquad \text{(HER)}, \tag{1b}$$

$$H_2O + 2h^+ \rightarrow \frac{1}{2}O_2 + 2H^+ \qquad \text{(OER)}. \tag{1c}$$

Electron transfer processes are critically important to drive the HER and OER given in Eq. (1). The electron transfer processes at the electrode–liquid junctions incur losses due to the concentration and kinetic overpotentials. The overpotential is the difference between the experimentally and theoretically observed values of the required voltages for water splitting in PECs. Among the mechanisms responsible for overpotential, η_a is the most critical and must be accounted for in HER and OER [59,60].

2.1. Modeling of activation overpotential

Activation overpotential (η_a), the most significant overpotential loss, is the potential difference above the equilibrium potential required to overcome the activation energy of the cell reaction to generate a specified current density. Basically, η_a causes a slow electrode reaction and is associated with the charge transfer between the electrode and the electrolytic solution. Therefore, it depends on the concentration of the electrolytic solution. The overpotential is measured from the difference between an electrode's equilibrium and operating potentials—the difference between the solid and dashed lines in Fig. 1. At an electrode–electrolytic solution junction, opposite polarity charges are accumulated, as shown in Fig. 1. The positive charge polarity exists in the electrolytic solution's inner Helmholtz plane. However, both positive and negative polarity charges exist in the outer Helmholtz plane. An electron participates in the initial reaction after passing through the inner Helmholtz plane. After coming out of the outer Helmholtz plane, the reaction between the electron and H^+ completes [61].

Considering the half-cell reactions of cathode and anode, the HER and OER can be written as

$$2H^+ + 2e^- \rightarrow H_2, \tag{2a}$$

$$O^{2-} \rightarrow \frac{1}{2}O_2 + 2e^-. \tag{2b}$$

If the equilibrium concentrations of H^+ and O^{2-} are denoted as C_{H^+} and $C_{O^{2-}}$, and the non-equilibrium concentrations of H^+ and O^{2-} are denoted as $C^*_{H^+}$ and $C^*_{O^{2-}}$, the Butler-Volmer equation (BVE) for the current density (J), due to the reactions in Eq. (2), can be written as [62]

$$J = J_0 \left[\frac{C_{H^+}}{C^*_{H^+}} \exp \frac{-\beta n F \eta}{RT} - \frac{C_{O^{2-}}}{C^*_{O^{2-}}} \exp \frac{(1-\beta) n F \eta}{RT} \right]. \tag{3}$$

In Eq. (3), J_0 is the exchange current density between the electrode and the electrolytic solution in equilibrium condition, n is the number of transferred electrons in HER, F is the Faraday constant, and R is the universal gas constant. Also, β is the symmetry factor of the electrode, which is usually assumed as 0.5 [5,63]. In PECs, J_0 can be defined as the equilibrium current density flowing equally in both directions at a reversible potential.

If the mass transfer coefficient between the electrode surface and the bulk electrolytic solution is greater than the HER rate, the concentration difference of H^+ is negligible between these two. In such a scenario, the mass transfer of ions between the electrolytic solution and the outer Helmholtz plane is much faster than the rate at which the ions react at the electrodes [64–66]. Therefore, we can write $C_{H^+} = C^*_{H^+}$, $C_{O^{2-}} = C^*_{O^{2-}}$, and $\eta = \eta_a$. Hence, the BVE becomes

$$J = J_0 \left[\exp \frac{-\beta n F \eta_a}{RT} - \exp \frac{(1-\beta) n F \eta_a}{RT} \right]. \tag{4}$$

The BVE given in Eq. (4) is not used at anode and cathode simultaneously. The properties of the anode and cathode materials and corresponding J_0 are not the same. Also, η_a is different for different electrochemical cells. Hence, it is simplified for two significant cases at the conditions during electrolysis related to (1) large overpotentials, when $|\eta_a| > 100$ mV, and (2) small overpotentials, $|\eta_a| < 10$ mV. The large overpotential approximation is used for water electrolysis as the optimum current density level is required to meet the minimum requirement of the redox potential. Therefore, the large cathodic or anodic overpotential is expected for water splitting [5,67].

For large cathodic activation overpotential ($\eta_{a,c}$), the second term of the BVE can be neglected as the sign of η_a is negative. When $J_0 = J_{0,c}$ is the cathodic exchange current density, Eq. (4) reduces to

$$\eta_{a,c} = \frac{RT}{\beta n F} \ln \left| \frac{J}{J_{0,c}} \right|. \tag{5}$$

In contrast, for large anodic activation overpotential ($\eta_{a,a}$), the first term of the BVE can be neglected as the sign of η_a is positive. When $J_0 = J_{0,a}$ is the anodic exchange current density, Eq. (4) reduces to

$$\eta_{a,a} = \frac{RT}{(1-\beta) n F} \ln \left| \frac{J}{J_{0,a}} \right|. \tag{6}$$

This work used Eqs. (5) and (6) to determine $\eta_{a,c}$ and $\eta_{a,a}$. The total η_a is the summation of $\eta_{a,c}$ and $\eta_{a,a}$.

2.2. STF efficiency

Photo-absorbing materials generate V_{oc} by absorbing solar irradiance spectrum in a PEC. If the number of electrolyzers (N_{elec}) is one, the voltage required for water splitting from photo-absorbing materials is the sum of water redox potential (E_{rxn}) and η_a. However, if there are multiple electrolyzers in a PEC, the minimum required voltage from a cell is $V_{oc} = N_{elec}(E_{rxn} + \eta_a)$.

The η_{STF} of a single electrolyzer system is given by $\eta_{STF} = \eta_f J E_{rxn}/P_{solar}$, where η_f is the Faradaic efficiency and P_{solar} is the power density of the solar irradiance spectrum. Faradaic efficiency defines the efficiency of photo-excited electron transfers between the electrode and electrolytic solution in electrochemical cells. Consequently, $\eta_{STF} = J E_{rxn}/P_{solar}$ for a water splitting process with 100% charge transfer efficiency, i.e., $\eta_f = 1$. If there are N_{elec} electrochemical cells in series, each will have the same J, and η_{STF} will be given by

$$\eta_{STF} = \frac{J \times N_{elec} \times E_{rxn}}{P_{solar}}. \tag{7}$$

This work takes a "detailed balance" approach to calculate J by using the standard ideal diode equation and the assumptions that (1) each cell is planar with an abrupt absorption threshold, (2) all photons with an energy greater than the bandgap are absorbed, and (3) there is no multiplication of carriers at the ambient condition and from radiative emission from other cells [40,47,68,69]. Therefore, one photon excites one electron, i.e., the PEC has a unity quantum efficiency [70]. Now, the current-voltage relationship of a single photo-absorber is given by

$$J = J_L - J_s[\exp(kV_{oc}/kT_a) - 1], \tag{8a}$$

$$J_L = q \int_{E_g}^{\infty} b_{AM\ 1.5G}\, dE, \tag{8b}$$

$$J_s = \frac{2 f_g q \pi}{h^3 c^2} \int_{E_g}^{\infty} \frac{E^2}{\exp(E/kT_a) - 1}\, dE, \tag{8c}$$

where J_L is the light-induced current density, J_s is the reverse saturation current density, and $b_{AM\ 1.5\ G}$ is the solar photon flux normal on the earth surface per energy interval dE. The constants q, h, c, and k are the elementary charge, Planck's constant, speed of light, and the Boltzmann constant, respectively.

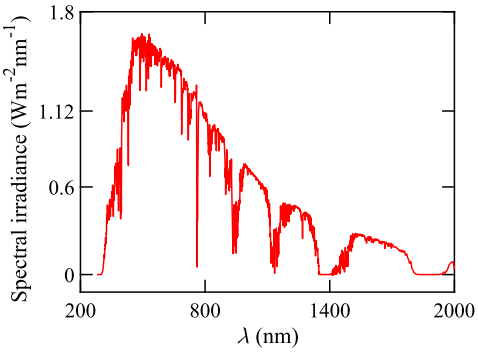

Fig. 2. AM 1.5 G terrestrial solar irradiance spectrum on the earth-surface.

Two kinds of losses occur when photo-absorbing materials absorb light: The radiative emission and the non-radiative transition [71]. The non-radiative transition is not considered here. The radiative emission is included as a geometric factor (f_g), which is equal to one when the radiative emission is limited to the front side, i.e., the photo-absorber has a perfect back reflector. In addition, $f_g = 2$ if the radiative emission can leave from both the front and back sides. Finally, unless stated otherwise, AM 1.5 G spectrum (ASTM G173), as shown in Fig. 2, and $T_a = 298.15$ K have been considered in this work [72].

2.3. Hydrogen production rate

HPR is an important performance parameter of an electrochemical cell. HPR depends on η_{STF} and the intensity of the solar irradiance spectrum (P_{total}) and can be calculated using [73]

$$\text{HPR (mol}H_2/\text{cm}^2\,\text{sec}) = \frac{N_{ph} \times \eta_{STF} \times P_{total}\ (\text{W cm}^{-2})}{\Delta G^0}, \tag{9}$$

where N_{ph} is the number of photo-absorbers. The HPR given in Eq. (9) is in per unit area of each photo-absorber. The total H_2 amount can be obtained by multiplying HPR by a single photo-absorber's effective photo-absorbing area. This work assumes that the effective photo-absorption area of each photo-absorber is the same. The unit of HPR is modified to mL H_2/cm^2 hour considering ambient temperature (T_a), pressure (P), and molar gas constant (R) by

$$\text{HPR (mL}H_2/\text{cm}^2\,\text{hour}) = \frac{\text{mol}H_2/\text{cm}^2\,\text{sec} \times R \times T_a \times 1\ \text{hour} \times 1000}{P}. \tag{10}$$

3. Simulation model

We have investigated several electrical and optical PEC configurations, such as electrically series or parallel, optically series or parallel, and mixed series and parallel. Figs. 3(a) and 3(b) show several electrical and optical PEC configurations. In an optically parallel configuration, photo-absorbing materials are positioned parallelly and not optically connected, thus splitting the solar light equally to each photo-absorber. The effective area of each photo-absorber is assumed to be the same, and the total effective area of all parallel photo-absorbers is calculated by summing up the effective areas of photo-absorbers. In contrast, light propagates from one photo-absorber to another for an optical series configuration. Hence, the effective area of every photo-absorbing material is considered one.

In an electrical configuration, the series connection increases V_{oc}, and the parallel connection increases J_{sc}. Different electrical configurations for PECs are shown in Fig. 3(b). Fig. 3(d) shows a PEC system where double photo-absorbing materials with double electrolyzers are connected optically and electrically in series.

We have calculated P_{solar} by integrating the solar irradiance spectrum considering wavelengths from 280 nm to 4000 nm. The simulations depend on the number of photo-absorbing materials and electrolyzers and the optical, electrical, and electrode configurations. The simulation parameters are given in Table 1. Additionally, we have assumed unity efficiency for the electrolyte to specifically focus on the impact of activation overpotential on the efficiency of PEC devices. Since J and η_a are related to each other, as given in Eqs. (5) and (6), we have solved them iteratively. We have calculated the initial J and V without η_a using Eq. (8) and estimated the initial $\eta_{a,c}$ and $\eta_{a,a}$ using Eqs. (5) and (6). Finally, J, V, $\eta_{a,c}$ and $\eta_{a,a}$ are determined from Eqs. (5), (6), and (8) using the numerical convergence method. Here, the total activation overpotential is $\eta_a = \eta_{a,c} + \eta_{a,a}$. Consequently, η_{STF} and HPR are calculated using Eqs. (7) and (10).

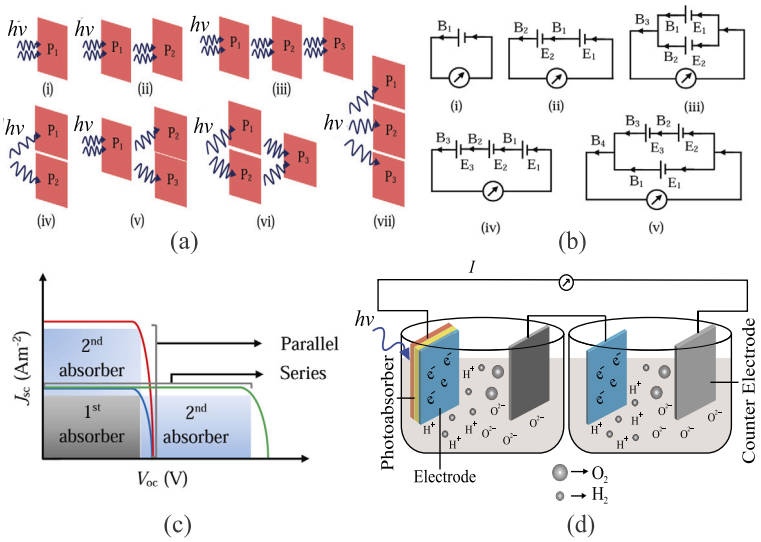

Fig. 3. (a) Different types of optical configurations: (i) single photo-absorbing material, (ii) series-connected double photo-absorbing materials, (iii) series-connected triple photo-absorbing materials, (iv) parallel-connected double photo-absorbing materials, (v, vi) mixture of series- and parallel-connected photo-absorbing materials, (vii) parallel-connected triple photo-absorbing materials. (b) Different types of electrical configurations: (i) single photo-absorbing material, (ii) series-connected double photo-absorbing materials, (iii) parallel-connected double photo-absorbing materials, (iv) series-connected triple photo-absorbing materials, (v) mixture of series- and parallel-connected photo-absorbing materials. (c) J_{sc} vs. V_{oc} characteristics of series and parallel photovoltaic cell. (d) Schematic diagram for double photo-absorbing materials with double electrolyzers in an optically series and electrically series configuration.

Table 1
Input parameters for the simulation model.

Name	Value	Name	Value
Temperature (T_a)	298.15 K	Pressure (P)	1 atm
Solar irradiance spectrum	AM 1.5 G	Faradaic efficiency (η_f)	1
Standard redox potential (E_{rxn})	1.23 V	Geometric factor (f_g)	1 or 2

Table 2
Electrode materials with their J_0 at T_a of 298.15 K in 1N H_2SO_4 solution.

Cathode	$J_{0,c}$ (Am^{-2})	Cathode	$J_{0,c}$ (Am^{-2})	Anode	$J_{0,a}$ (Am^{-2})
Palladium (Pd)	10	Titanium (Ti)	7.00×10^{-4}	PtFe/C	2.15×10^{-3}
Platinum (Pt)	8	Lead (Pb)	1.00×10^{-8}	PtW_2C/C	4.70×10^{-4}
Nickel (Ni)	0.07	Cadmium (Cd)	1.50×10^{-7}	Ru_xSe_y	2.22×10^{-4}
Gold (Au)	0.04	Manganese (Mn)	1.30×10^{-7}	$Ru_xFe_ySe_z$	4.47×10^{-4}
Tungsten (W)	0.013	Mercury (Hg)	5.00×10^{-10}	Pt	1.00×10^{-5}

3.1. Electrode material library

Electrode materials used in this work for H_2 production and their corresponding J_0 are shown in Table 2. Ten materials are used as cathodes and five materials are used as anodes. The J_0 values given in Table 1 are constant considering T_a of 298.15 K and 1 N H_2SO_4 electrolytic solution [74,75]. This work utilized these materials to calculate η_a for different PEC configurations.

3.2. Photo-absorbing material library

Photo-absorbing materials used in this work for H_2 production and their corresponding E_g values are shown in Table 3 [5,76]. This work analyzes the state of H_2 production in different PEC combinations using these 30 materials with E_g varying from 0.52 eV to 3.08 eV.

4. Results and discussion

4.1. Activation overpotential in PECs

In PECs, η_a critically depends on J_{sc}, which is calculated from E_g of the photo-absorbing material. In addition, different electrode pairs show a significant variation of η_a due to the difference of J_0 among them. Fig. 4 shows η_a vs. E_g and J_{sc} of a photo-absorber

Table 3
Photo-absorbing materials and their corresponding bandgap energy (E_g).

Photo-absorber	E_g (eV)	Photo-absorber	E_g (eV)	Photo-absorber	E_g (eV)
C-Si/$CuSnS_4$	0.52	p-GaAs/Cu_2MnSnS_4	1.4	Cu_4SiS_4	1.95
Ge	0.67	$Cu_2ZnSnSe_4$	1.48	Cu_3SbSe_3	2.01
$BaSi_2$	0.72	$Cu_2BaSnSSe_3$	1.59	Cu_2O	2.06
$Cu_2ZnSnSe_4$	0.9	$CuBiS_2$	1.61	Cu_2ZnGeS_4	2.08
$CuSbTe_2$	0.92	$Cu_2BaSnSe_4$	1.68	Cu_3SbS_3	2.13
$CuSbSe_2$	1.05	Cu_2FeSnS_4	1.71	n-Fe_2O_3	2.2
Cu_4GeS_4	1.15	Cu_2BeSnS_4	1.76	p-GaP	2.3
$CuBiSe_2$	1.18	Cu_2BaSnS_4	1.8	$Cd_{0.6}Zn_{0.4}S$	2.47
p-InP	1.3	Cu_2SrSnS_4	1.81	Penta-C_{20}/Cu_2ZnSiS_4	2.89
$CuSbS_2$	1.37	Cu_3BiS_3	1.88	ZnO-Ce	3.08

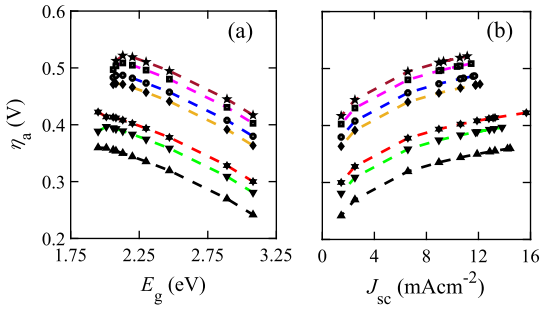

Fig. 4. Activation overpotential (η_a) vs. bandgap (E_g) and short circuit current density (J_{sc}) for various electrode pairs. Electrode pairs are denoted by different markers: ★ indicates Au cathode and PtW_2C/C anode, ■ indicates Ni cathode and PtW_2C/C anode, ● indicates Pt cathode and Pt anode, ◆ indicates Ni cathode and PtFeC/C anode, ✶ indicates Pt cathode and Ru_xSe_y anode, ▼ indicates Pt cathode and PtW_2C/C anode, and ▲ indicates Pt cathode and PtFe/C anode.

for various electrode pairs. Fig. 4(a) shows that η_a decreases as the photo-absorber E_g increases, which is attributed to increasing V_{oc} and decreasing J_{sc} as E_g increases, as shown in Fig. 3(c). By contrast, η_a increases with J_{sc}, as shown in Fig. 4(b).

The smallest η_a values are found for Pt cathode and PtFe/C anode with the variation of E_g. On the other hand, the greatest η_a values are found for the Au cathode and PtW_2C/C anode. The Pt and PtFe/C electrode pair has a greater J_0 than Au and PtW_2C/C electrode pair. Hence, the charge transfer kinetics of the Pt and PtFe/C electrode pair is faster than the other.

Electrical configurations can have photo-absorbers in different branches along with the electrodes. Different electrical configurations are possible for electrodes placed on different branches, as shown in Fig. 3(b). Fig. 5 shows that there are significant changes in η_a based on the electrode position due to the change in J_{sc} from branch to branch. Therefore, η_{STF} and HPR also vary with the electrode position, making the electrode pair configuration a critical design parameter for H_2 production.

This work analyzed the impacts of electrical series and parallel configurations by considering a mixed PEC configuration, as shown in Fig. 3(b)(v), where four electrical branches are present. Fig. 5 shows η_a against E_g of photo-absorbers in different branches. The bandgaps E_{g2} and E_{g3} of photo-absorbers are the same due to optically parallel connection. In Figs. 5(a) and (b), E_{g2} and E_{g3} are varied equally, while keeping E_{g1} fixed. In all cases, η_a is maximum at branch 4 and minimum at branch 1 since η_a is proportional to J_{sc}. Therefore, η_a is less in branch 1 as J_{sc} is the smallest in branch 1 among all branches. The same feature is also observed in branches 2 and 3 where J_{sc} is greater than that of branch 1. Since J_{sc} of branch 4 is the summation of J_{sc} of branches 1, 2, and 3, the maximum η_a occurs at branch 4. In Figs. 5(c) and (d), E_{g1} is varied while keeping E_{g2} and E_{g3} fixed, and a similar change in J_{sc} has been obtained. The features shown in Fig. 5 show the electrical branch where the electrode should be placed so that the optimized η_{STF} and HPR are found.

η_a impacts η_{STF} of any PEC significantly. Due to the presence of η_a, a higher potential is needed to split water than in an ideal situation. Eventually, J_{sc}, on which η_{STF} depends proportionally, decreases. Therefore, η_{STF} decreases as well with η_a. Fig. 6 shows η_{STF} against E_g and J_{sc} with and without η_a. In both cases, the PEC consists of a single photo-absorbing material and a single electrolyzer. The electrolyzer uses Pt as the cathode and PtFe/C as the anode. When $\eta_a = 0$, η_{STF} can be up to 30%. However, η_{STF} drops to 18% when η_a is considered. Notably, $\eta_{STF} = 0$ for $E_g = 1.59$–1.96 V if η_a is considered, although $\eta_{STF} \gg 0$ if η_a is not considered. Fig. 6(b) shows that a higher η_{STF} is achieved for a smaller E_g since J_{sc} increases when E_g decreases. Since J_0 is fixed for a particular electrode pair, η_a varies with J_{sc} following Eqs. (5) and (6).

4.2. Choice of electrode materials

In this work, PEC performances are analyzed for different electrode pairs. The choice of the proper electrode pair is essential as η_a depends on it. A greater η_{STF} with a suitable E_g is obtained for an electrode pair if η_a is less. Fig. 7 shows η_{STF} for different electrode pairs considering η_a. Fig. 7(a) shows η_{STF} for different pairs of electrode materials for a single photo-absorber, while Fig. 7(b) shows that for double photo-absorbers connected in series both electrically and optically. Here, $E_g = 2.13$ eV is used for the single photo-

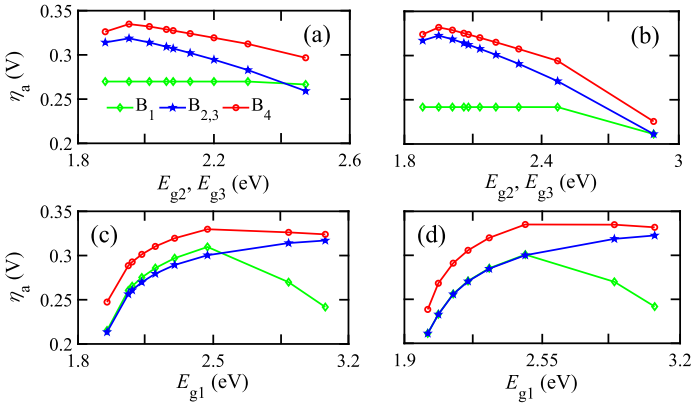

Fig. 5. η_a vs. energy bandgaps of photo-absorbers for optical series and electrical series configuration of single photo-absorbing material with parallel-connected double photo-absorbing materials. Electrodes are located in different branches (B_1, B_2, B_3, and B_4) of the electrical configuration. (a) E_{g2} and E_{g3} are varied while E_{g1} is constant at 3.08 eV, (b) E_{g2} and E_{g3} are varied while E_{g1} is kept constant at 2.88 eV, (c) E_{g1} is varied while E_{g2} and E_{g3} are kept constant at 1.88 eV, and (d) E_{g1} is varied while E_{g2} and E_{g3} are kept constant at 1.95 eV.

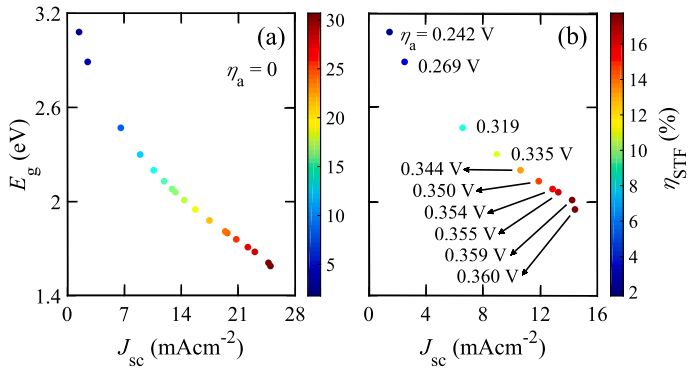

Fig. 6. η_{STF} against E_g for a single photo-absorbing material in a single electrolyzer (a) without and (b) with considering η_a. In each case, Pt is used as the cathode and PtFe/C is used as the anode. η_a values are shown in (b) beside corresponding data points.

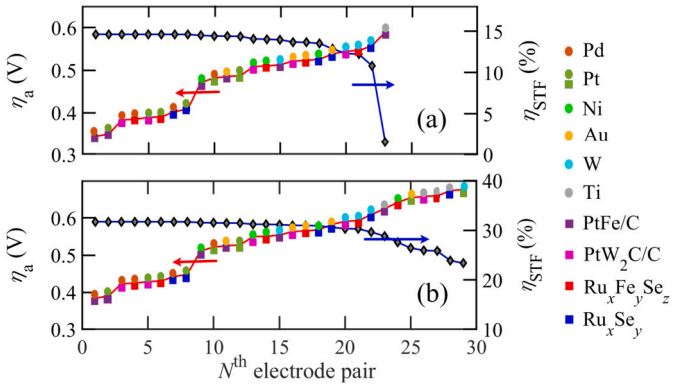

Fig. 7. η_a and η_{STF} for (a) single photo-absorber with $E_g = 2.13$ eV and (b) double photo-absorbers with $E_{g1} = 1.4$ eV and $E_{g2} = 0.72$ eV. Symbols ● and ■ indicate cathode and anode, respectively. Electrode materials are given as legends.

absorber, and $E_g = 1.4$ eV and 0.72 eV are used in double photo-absorbers. Fig. 7 shows that η_a and η_{STF} depend inversely on each other. If η_a increases, η_{STF} decreases for any pair of cathode and anode. As a result, for the anode and cathode materials considered, the bottom left pairs of Fig. 7 can be preferable for any PECs as they have a smaller η_a due to larger J_0. Fig. 7(b) shows that η_{STF} depends more sensitively on the choice of electrode materials for double photo-absorbers than a single photo-absorber in a PEC configuration.

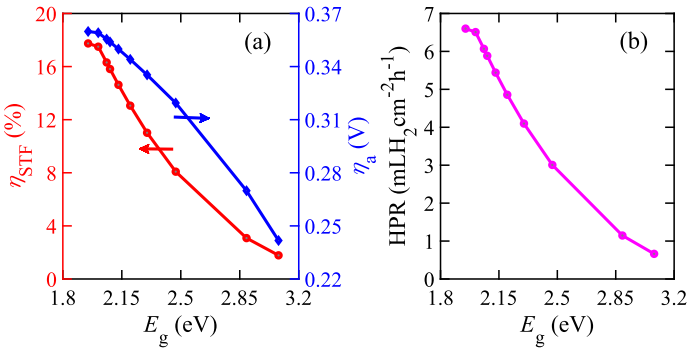

Fig. 8. (a) η_{STF} and η_a vs. E_g and (b) HPR vs. E_g of a PEC with a single photo-absorber in an electrolyzer.

4.3. PEC configurations

HPR and η_{STF} are calculated considering η_a utilizing photo-absorbing and electrode materials from the libraries. η_{STF} depends on different optical and electrical configurations of PEC. η_{STF} also depends on the number of photo-absorbers, number of electrolyzers, and different electrode pairs. Increasing the number of photo-absorbers increases the absorption of solar energy. Although η_a increases when more electrolyzers are added to the system, the negative gradient of H_2 concentration decreases, offering convenient H_2 collection. This work compares η_{STF} of each photo-absorbing material utilizing several electrolyzers and electrode pairs.

4.3.1. Single photo-absorber

Fig. 8 shows η_{STF}, η_a, and HPR for a PEC that has a single photo-absorber in an electrolyzer. This PEC has a Pt cathode and a PtFe/C anode. We vary the photo-absorber E_g as given in Table 3. In this case, Fig. 8(a) shows that the maximum η_{STF} is 17.743% when the photo-absorber $E_g = 1.95$ eV and its corresponding η_a is 0.35982 V. Murphy et al. also reported that the required minimum E_g is almost 2 eV by utilizing AM 1.5 G for single photo-absorber [77]. If η_a is not considered, $\eta_{STF} = 19.337\%$ for the same E_g, as also reported in Ref. 37. We note that $\eta_{STF} = 0$ for $E_g < 1.9$ eV if η_a is considered. However, η_{STF} can be obtained for smaller E_g values if η_a is neglected. For example, when $E_g = 1.59$ eV, η_{STF} is 30.68% without including η_a. However, $\eta_{STF} = 0$ for the same bandgap, i.e., $E_g = 1.59$ eV, when η_a is considered in the calculation as the photo-absorber E_g does not meet the required potential for water splitting. Figs. 8(a) and (b) show that η_{STF} and HPR decrease when E_g increases. This is because η_{STF} is proportional to J_{sc}, which decreases with increasing E_g. Since HPR is proportional to η_{STF}, it has a similar trend. On the other hand, η_a decreases when E_g increases as it also depends proportionally on J_{sc}.

4.3.2. Double photo-absorbers

We have also analyzed the impact of η_a on η_{STF} for double photo-absorbing materials in a PEC. Four PEC configurations are possible with double photo-absorbers, as shown in Figs. 3(a) and (b). This work investigated only the optical series-electrical series (OS-ES) and optical parallel-electrical series (OP-ES) PEC configurations for double photo-absorbers. Other configurations, such as optical series-electrical parallel (OS-EP) and optical parallel-electrical parallel (OP-EP) are discussed with triple photo-absorbers.

Fig. 9 shows the impact of η_a on η_{STF} for OS-ES PEC configuration with double photo-absorbers. While Figs. 9(a) and (b) illustrate η_{STF} and η_a with E_g for single electrolyzer, Figs. 9(c) and (d) illustrate those for double electrolyzers. For the single electrolyzer, Pt is used as the cathode and PtFe/C is used as the anode. In Figs. 9(a) and (c), the maximum η_{STF} is observed in the left-bottom portion of the range of the bandgaps, showing the maximum power point (MPP), where the cell outputs the maximum net power at a certain V_{oc} and J_{sc}. As E_g increases, V_{oc} also increases but J_{sc} decreases. As a result, at a certain combination of the bandgaps, the MPP is achieved with the maximum η_{STF}. In most cases, η_{STF} does not change significantly. J_{sc} is approximately a constant till the MPP, however, it decreases significantly as the operating point crosses the MPP. Therefore, the output power (P_{out}) and η_{STF} decreases according to

$$V_{oc} = V_{oc1} + V_{oc2}, \qquad P_{out} = V_{oc} J_{sc}, \qquad \eta_{STF} = \frac{P_{out}}{P_{in}}. \tag{11}$$

In the double-photo-absorber configuration, $V_{oc} = V_{oc1} + V_{oc2}$, according to Eq. (11). However, V_{oc1} of E_{g1} acts as the main driver. When E_{g2} increases linearly, keeping E_{g1} constant, change of η_{STF} is also shown in Figs. 9(a) and (c). η_{STF} sharply decreases as E_{g2} increases for $E_{g1} \leq 2.6$ eV. However, when $E_{g1} > 2.6$ eV, η_{STF} does not change much when E_{g2} increases.

We note that E_{g1} and E_{g2} used in Fig. 9 are chosen from the photo-absorber library given in Table 3. Here, an increase in E_g means an increase in V_{oc}. Keeping E_{g1} constant means keeping V_{oc1} constant for the first photo-absorber, and an increase in E_{g2} will not impact η_{STF} as J_{sc} remains constant initially, as shown in Fig. 3(c). When E_{g2} continues to increase, it eventually overcomes the constant value of E_{g1}, and as a result, J_{sc} decreases. Consequently, η_{STF} decreases as well. These phenomena are observed in Fig. 9(a). η_a values for the variations of E_{g1} and E_{g2} are shown in Fig. 9(b). Fig. 9(c) shows η_{STF} for the same configuration as before, except for a PEC with double electrolyzers. Fig. 9(c) also shows that η_{STF} values are right-shifted compared to that in Fig. 9(a) due to high V_{oc} required for water splitting in double electrolyzers. Hence, the E_g range for double electrolyzers is smaller than that of

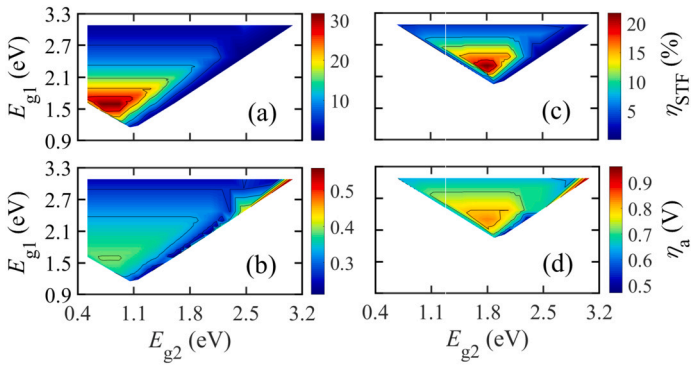

Fig. 9. Optimized η_{STF} and corresponding η_a for double photo-absorbing materials with optical and electrical series configuration for (a,b) single electrolyzer and (c,d) for double electrolyzers.

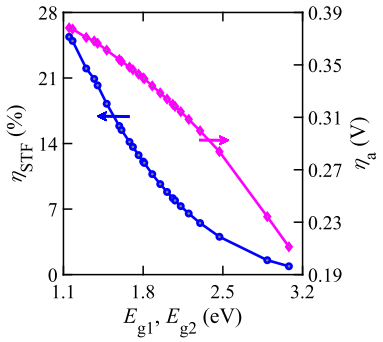

Fig. 10. η_{STF} and η_a vs. bandgaps for optical parallel and electrical series configuration with double photo-absorbing materials in a single electrolyzer.

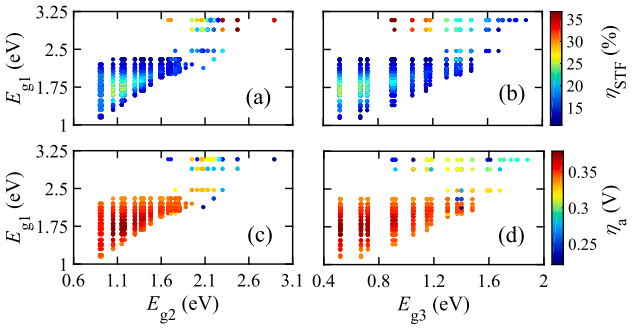

Fig. 11. Optimized η_{STF} in (a,b) and corresponding η_a in (c,d) are shown for triple photo-absorbing materials with optical series and electrical series configuration.

a single electrolyzer. The second electrode pair of the double electrolyzers consists of Ni as the cathode and PtW_2/C as the anode. Corresponding η_a is shown in Fig. 9(d), where the values of η_a are higher than single electrolyzer values due to double electrolyzer.

Fig. 10 presents η_{STF} and η_a for OP-ES connection of double photo-absorbers in a single electrolyzer. The electrode pair consists Pt as the cathode and PtFe/C as the anode. The bandgap of each photo-absorber must be the same for an optically parallel connection. Fig. 10 shows that η_{STF} decreases as E_g increases. For double electrolyzers, higher bandgaps are required for water splitting to obtain η_{STF} along with decreasing η_a.

4.3.3. Triple photo-absorbers

Fig. 11 is a scatter plot of η_{STF} and η_a for OS-ES PEC configuration with triple photo-absorbing materials in a single electrolyzer. Figs. 11(a,b) and 11(c,d) are illustrations of η_{STF} and η_a against E_g, respectively. The electrode pair consists of Pt as the cathode and PtFe/C as the anode. We note that $\eta_{STF} \geq 30\%$ when $E_{g1} \geq 2.89$ eV, $2.3 \leq E_{g2} \leq 2.89$ eV, and $0.9 \leq E_{g3} \leq 1.18$ eV. Fig. 11 also gives an idea of η_{STF} for any compatible bandgaps of triple photo-absorbing materials compared to the color from the color bar. The advantage of using triple photo-absorbing materials rather than single or double photo-absorbing materials is that the lower bandgap values can be utilized, and a greater η_{STF} can be obtained in the presence of η_a. For a PEC with double electrolyzers, although the range of bandgaps for photo-absorbers increases, η_a increases as well.

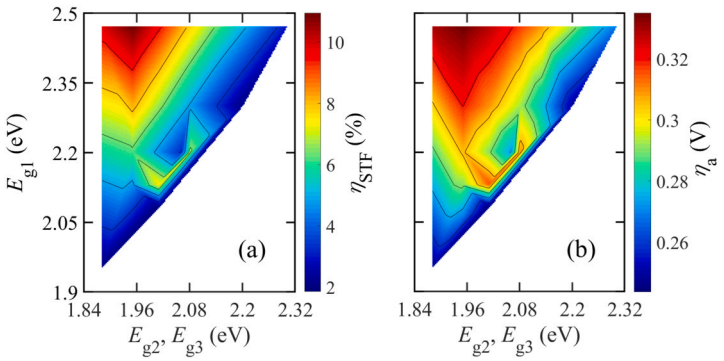

Fig. 12. (a) Variation of η_{STF} with bandgap for the mixed configuration analyzed in this paper. (b) Corresponding η_a for same PEC configuration.

Table 4
Optimized η_{STF} and HPR including η_a for different PEC configurations of Fig. 3(a,b).

Configuration	N_{elec}	Cathode	Anode	E_g (eV)	η_{STF} (%)	HPR	η_a (V)
Fig. 3(a)(i), 3(b)(i)	1	Pt	PtFe/C	1.95	17.74	6.60	0.359
Fig. 3(a)(ii),	1	Pt	PtFe/C	1.59, 0.92	31.75	23.62	0.389
3(b)(ii)	2	Pt, Ni	PtFe/C, PtW_2C/C	2.3, 1.81	21.891	16.28	0.831
	3	Pt, Ni, Au	PtFe/C, PtFe/C, PtW_2C/C	3.08, 2.47	5.23	3.89	1.017
Fig. 3(a)(iv),	1	Pt	PtFe/C	1.15, 1.15	25.39	18.89	0.378
3(b)(ii)	2	Pt, Ni	PtFe/C, PtW_2C/C	2.01, 2.01	16.51	12.28	0.802
	3	Pt, Pt, Ni	PtFe/C, PtFe/C, PtW_2C/C	2.89, 2.89	4.621	3.44	0.863
Fig. 3(a)(iii),	1	Pt	PtFe/C	3.08, 2.47, 0.90	36.75	41.02	0.242
3(b)(iv)	2	Pt, Ni	PtFe/C, PtW_2C/C	2.01, 1.48, 1.05	35.30	29.40	0.880
	3	Pt, Ni, Au	PtFe/C, PtFe/C, PtW_2C/C	2.47, 2.06, 1.76	24.24	27.06	1.255
Fig. 3(a),	1	Pt	PtFe/C	0.92, 0.92, 0.92	21.28	23.75	0.369
3(b)(iv)	2	Pt, Ni	PtFe/C, PtW_2C/C	1.48, 1.48, 1.48	23.97	26.75	0.840
	3	Pt, Pt, Ni	PtFe/C, PtFe/C, PtW_2C/C	1.95, 1.95, 1.95	17.57	19.61	1.069
Fig. 3(a)(v), 3(b)(v)	1	Pt	PtFe/C	2.47, 1.95, 1.95	10.95	12.22	0.335

For the OP-ES PEC configuration of triple photo-absorbing materials, η_{STF} and η_a follow a similar trend as in the OP-ES PEC configuration of double photo-absorbing materials. However, smaller bandgap materials can be used in triple photo-absorbing materials.

We also investigated a mixed configuration to obtain a detailed analysis of EP PEC configuration. For the mixed configuration of triple photo-absorbing materials, we used the optical configuration from Fig. 3(a)(v) and the electrical configuration from Fig. 3(b)(v). J_{sc} will increase in the EP configuration, whereas V_{oc} will increase in the ES configuration. There are four branches in this mixed configuration. One branch is external, and the rest are internal. The mixed configuration will work fine when an electrolyzer is located in the external branch according to the connections of Fig. 3(b)(v). However, when an electrolyzer is located in the internal branch, then another electrolyzer should be placed in the external branch. Otherwise, the external connection must be open to make the circuitry work, and opening the external connection will eventually make the mixed configuration an ES configuration.

We analyzed η_{STF} and η_a with E_g for the mixed configuration where a single electrolyzer is located in the external branch, as shown in Fig. 12. η_{STF} and η_a show a similar trend where larger values of them are obtained on the top-left portion of the Figs. 12(a) and (b) with $E_{g1} \geq 2.2$ eV and E_{g2}, $E_{g3} \leq 2.2$ eV. The results we obtained here are also applicable for the EP PEC configuration where E_{g1} is connected in parallel with series connected E_{g2} and E_{g3}.

Table 4 is a summary of the optimized η_{STF} and HPR for different PEC configurations, as shown in Figs. 3(a) and 3(b). For each PEC configuration with several electrolyzers, the optimized cathode, anode, and photo-absorbing materials are found from the photo-absorbing and electrode material libraries based on η_{STF} given in Table 4. Corresponding HPR and η_a are also given in Table 4.

5. Conclusion

This work is critical to calculating η_{STF} and HPR in realistic PECs. This work includes η_a in calculating η_{STF} and HPR for different configurations and finds photo-absorber and electrode materials for desired PEC performances. It is found that the η_{STF} and HPR are significantly affected when η_a is considered in the calculation. An idea is obtained for selecting appropriate photo-absorbers and electrode pairs for PEC configurations to achieve a desired η_{STF} and HPR. The proper design of electrical branches and the positions of electrodes in branches can be determined based on the optimized η_{STF} and HPR calculated in the presence of η_a. However, it

is important to note that this work considers a constant temperature and pressure. This work also does not consider losses due to electrolytes. The results will vary slightly when the impacts of temperature, pressure, and electrolytic losses are considered.

CRediT authorship contribution statement

Abdul Ahad Mamun, Asif Billah: conceived and designed the experiments; performed the experiments; analyzed and interpreted the data; Contributed reagents, materials, analysis tools or data; and wrote the paper.
Muhammad Anisuzzaman Talukder: conceived and designed the experiments; performed the experiments; analyzed and interpreted the data; and wrote the paper.

Declaration of competing interest

The authors declare that they have no known competing financial interests or personal relationships that could have appeared to influence the work reported in this paper.

Data availability

Data will be made available on request.

References

[1] B.D. James, G.N. Baum, J. Perez, K.N. Baum, Technoeconomic analysis of photoelectrochemical (PEC) hydrogen production, DOE Report, 2009.
[2] L.M. Peter, K. Upul Wijayantha, Photoelectrochemical water splitting at semiconductor electrodes: fundamental problems and new perspectives, ChemPhysChem 15 (10) (2014) 1983–1995.
[3] S. Linic, P. Christopher, D.B. Ingram, Plasmonic-metal nanostructures for efficient conversion of solar to chemical energy, Nat. Mater. 10 (12) (2011) 911–921.
[4] Y.J. Jang, J.S. Lee, Photoelectrochemical water splitting with p-type metal oxide semiconductor photocathodes, ChemSusChem 12 (9) (2019) 1835–1845.
[5] M.G. Walter, E.L. Warren, J.R. McKone, S.W. Boettcher, Q. Mi, E.A. Santori, N.S. Lewis, Solar water splitting cells, Chem. Rev. 110 (11) (2010) 6446–6473.
[6] P. Dias, A. Mendes, Hydrogen production from photoelectrochemical water splitting, in: R.A. Meyers (Ed.), Encyclopedia of Sustainability Science and Technology, Springer Science and Business Media LLC, Berlin/Heidelberg, Germany, 2017, pp. 1–52.
[7] D. Welsby, J. Price, S. Pye, P. Ekins, Unextractable fossil fuels in a 1.5 C world, Nature 597 (7875) (2021) 230–234.
[8] T.U.I.P. on Climate Change (IPCC), UN Climate Change Conference (cop26), Glasgow, United Nations, October-November 2021.
[9] K.D. Kadam, H. Kim, S. Rehman, H. Patil, J. Aziz, T.D. Dongale, M.F. Khan, D.-k. Kim, Optimization of ZnO: PEIE as an electron transport layer for flexible organic solar cells, Energy Fuels 35 (15) (2021) 12416–12424.
[10] K.D. Kadam, H. Kim, S. Rehman, H. Patil, J. Aziz, T.D. Dongale, M.F. Khan, D.-k. Kim, Compositional dynamics of the electron transport layer (ZnO: PEIE) in P3HT: $PC_{61}BM$ organic solar cells, Mater. Sci. Semicond. Process. 136 (2021) 106118.
[11] S.S. Sutar, S.M. Patil, S.J. Kadam, R.K. Kamat, D.-k. Kim, T.D. Dongale, Analysis and prediction of hydrothermally synthesized ZnO-based dye-sensitized solar cell properties using statistical and machine-learning techniques, ACS Omega 6 (44) (2021) 29982–29992.
[12] M. Gaikwad, M. Suryawanshi, P. Maldar, T. Dongale, A. Moholkar, Nanostructured zinc oxide photoelectrodes by green routes M-SILAR and electrodeposition for dye sensitized solar cell, Opt. Mater. 78 (2018) 325–334.
[13] S. Fakourian, A theoretical study on overpotential and photocurrent of a photo fuel cell, Theor. Found. Chem. Eng. 53 (1) (2019) 147–150.
[14] L. Dunyushkina, A. Pavlovich, A. Khaliullina, Activation of porous Pt electrodes deposited on YSZ electrolyte by nitric acid treatment, Materials 14 (18) (2021) 5463.
[15] P. Varadhan, H.-C. Fu, Y.-C. Kao, R.-H. Horng, J.-H. He, An efficient and stable photoelectrochemical system with 9% solar-to-hydrogen conversion efficiency via InGaP/GaAs double junction, Nat. Commun. 10 (1) (2019) 1–9.
[16] P. Cendula, L. Steier, P.A. Losio, M. Grätzel, J.O. Schumacher, Analysis of optical losses in a photoelectrochemical cell: a tool for precise absorptance estimation, Adv. Funct. Mater. 28 (1) (2018) 1702768.
[17] A. Fujishima, K. Honda, Electrochemical photolysis of water at a semiconductor electrode, Nature 238 (5358) (1972) 37–38.
[18] Y. Chen, X. Feng, Y. Liu, X. Guan, C. Burda, L. Guo, Metal oxide-based tandem cells for self-biased photoelectrochemical water splitting, ACS Energy Lett. 5 (3) (2020) 844–866.
[19] A. Crovetto, R. Nielsen, E. Stamate, O. Hansen, B. Seger, I. Chorkendorff, P.C. Vesborg, Wide band gap Cu_2SrSnS_4 solar cells from oxide precursors, ACS Appl. Energy Mater. 2 (10) (2019) 7340–7344.
[20] K. Zhang, M. Ma, P. Li, D.H. Wang, J.H. Park, Water splitting progress in tandem devices: moving photolysis beyond electrolysis, Adv. Energy Mater. 6 (15) (2016) 1600602.
[21] J.S. Santos, P. d, S. Araújo, Y.B. Pissolitto, P.P. Lopes, A.P. Simon, M. d, S. Sikora, F. Trivinho-Strixino, The use of anodic oxides in practical and sustainable devices for energy conversion and storage, Materials 14 (2) (2021) 383.
[22] W. Yang, R.R. Prabhakar, J. Tan, S.D. Tilley, J. Moon, Strategies for enhancing the photocurrent, photovoltage, and stability of photoelectrodes for photoelectrochemical water splitting, Chem. Soc. Rev. 48 (19) (2019) 4979–5015.
[23] S. Hu, C. Xiang, S. Haussener, A.D. Berger, N.S. Lewis, An analysis of the optimal band gaps of light absorbers in integrated tandem photoelectrochemical water-splitting systems, Energy Environ. Sci. 6 (10) (2013) 2984–2993.
[24] B. Seger, O. Hansen, P.C. Vesborg, A flexible web-based approach to modeling tandem photocatalytic devices, Sol. Rrl 1 (1) (2017) e201600013.
[25] A. Pusch, P. Pearce, N.J. Ekins-Daukes, Analytical expressions for the efficiency limits of radiatively coupled tandem solar cells, IEEE J. Photovolt. 9 (3) (2019) 679–687.
[26] T. Jafari, E. Moharreri, A.S. Amin, R. Miao, W. Song, S.L. Suib, Photocatalytic water splitting—the untamed dream: a review of recent advances, Molecules 21 (7) (2016) 900.
[27] T.J. Jacobsson, V. Fjällström, M. Sahlberg, M. Edoff, T. Edvinsson, A monolithic device for solar water splitting based on series interconnected thin film absorbers reaching over 10% solar-to-hydrogen efficiency, Energy Environ. Sci. 6 (12) (2013) 3676–3683.
[28] S.S. Kalanur, L.T. Duy, H. Seo, Recent progress in photoelectrochemical water splitting activity of WO_3 photoanodes, Top. Catal. 61 (9) (2018) 1043–1076.
[29] C. Jiang, S.J. Moniz, A. Wang, T. Zhang, J. Tang, Photoelectrochemical devices for solar water splitting–materials and challenges, Chem. Soc. Rev. 46 (15) (2017) 4645–4660.
[30] Z. Wang, L. Wang, Photoelectrode for water splitting: materials, fabrication and characterization, Sci. China Mater. 61 (6) (2018) 806–821.

[31] Y. Yang, S. Niu, D. Han, T. Liu, G. Wang, Y. Li, Progress in developing metal oxide nanomaterials for photoelectrochemical water splitting, Adv. Energy Mater. 7 (19) (2017) 1700555.
[32] X. Wang, Y. Zhang, J. Li, G. Liu, M. Gao, S. Ren, B. Liu, L. Zhang, G. Han, J. Yu, et al., Platinum cluster/carbon quantum dots derived graphene heterostructured carbon nanofibers for efficient and durable solar-driven electrochemical hydrogen evolution, Small Methods 6 (4) (2022) 2101470.
[33] A.P. Alivisatos, Semiconductor clusters, nanocrystals, and quantum dots, Science 271 (5251) (1996) 933–937.
[34] L. Jin, H. Zhao, Z.M. Wang, F. Rosei, Quantum dots-based photoelectrochemical hydrogen evolution from water splitting, Adv. Energy Mater. 11 (12) (2021) 2003233.
[35] Z. Liang, H. Hou, Z. Fang, F. Gao, L. Wang, D. Chen, W. Yang, Hydrogenated TiO_2 nanorod arrays decorated with carbon quantum dots toward efficient photoelectrochemical water splitting, ACS Appl. Mater. Interfaces 11 (21) (2019) 19167–19175.
[36] G. Liu, X. Wang, B. Liu, G. Han, W. Jiang, Y. Zhang, H. Zhao, Band engineering enables highly efficient and stable photoelectrochemical hydrogen evolution, Chem. Eng. J. 450 (2022) 137813.
[37] I. Holmes-Gentle, K. Hellgardt, A versatile open-source analysis of the limiting efficiency of photo electrochemical water-splitting, Sci. Rep. 8 (1) (2018) 1–9.
[38] Y.-R. He, F.-F. Yan, H.-Q. Yu, S.-J. Yuan, Z.-H. Tong, G.-P. Sheng, Hydrogen production in a light-driven photoelectrochemical cell, Appl. Energy 113 (2014) 164–168.
[39] M.F. Weber, M.J. Dignam, Efficiency of splitting water with semiconducting photoelectrodes, J. Electrochem. Soc. 131 (6) (1984) 1258.
[40] K.T. Fountaine, H.J. Lewerenz, H.A. Atwater, Efficiency limits for photoelectrochemical water-splitting, Nat. Commun. 7 (1) (2016) 1–9.
[41] M.T. Spitler, M.A. Modestino, T.G. Deutsch, C.X. Xiang, J.R. Durrant, D.V. Esposito, S. Haussener, S. Maldonado, I.D. Sharp, B.A. Parkinson, et al., Practical challenges in the development of photoelectrochemical solar fuels production, Sustain. Energy Fuels 4 (3) (2020) 985–995.
[42] L.C. Seitz, Z. Chen, A.J. Forman, B.A. Pinaud, J.D. Benck, T.F. Jaramillo, Modeling practical performance limits of photoelectrochemical water splitting based on the current state of materials research, ChemSusChem 7 (5) (2014) 1372–1385.
[43] R. Sathre, J.B. Greenblatt, K. Walczak, I.D. Sharp, J.C. Stevens, J.W. Ager, F.A. Houle, Opportunities to improve the net energy performance of photoelectrochemical water-splitting technology, Energy Environ. Sci. 9 (3) (2016) 803–819.
[44] R.E. Rocheleau, E.L. Miller, Photoelectrochemical production of hydrogen: engineering loss analysis, Int. J. Hydrog. Energy 22 (8) (1997) 771–782.
[45] W. Shockley, H.J. Queisser, Detailed balance limit of efficiency of p-n junction solar cells, J. Appl. Phys. 32 (3) (1961) 510–519.
[46] J.R. Bolton, S.J. Strickler, J.S. Connolly, Limiting and realizable efficiencies of solar photolysis of water, Nature 316 (6028) (1985) 495–500.
[47] M. Hanna, A. Nozik, Solar conversion efficiency of photovoltaic and photoelectrolysis cells with carrier multiplication absorbers, J. Appl. Phys. 100 (7) (2006) 074510.
[48] Y. Xu, T. Gong, J.N. Munday, The generalized Shockley-Queisser limit for nanostructured solar cells, Sci. Rep. 5 (1) (2015) 1–9.
[49] M.L. Buhl Jr, R.E. Bird, R.V. Bilchak, J.S. Connolly, J.R. Bolton, Thermodynamic limits on conversion of solar energy to work or stored energy—effects of temperature, intensity and atmospheric conditions, Sol. Energy 32 (1) (1984) 75–84.
[50] L.C. Hirst, N.J. Ekins-Daukes, Fundamental losses in solar cells, Prog. Photovolt. 19 (3) (2011) 286–293.
[51] M.T. Patel, M.R. Khan, M.A. Alam, Thermodynamic limit of solar to fuel conversion for generalized photovoltaic–electrochemical systems, IEEE J. Photovolt. 8 (4) (2018) 1082–1089.
[52] S. Chu, W. Li, Y. Yan, T. Hamann, I. Shih, D. Wang, Z. Mi, Roadmap on solar water splitting: current status and future prospects, Nano Futures 1 (2) (2017) 022001.
[53] N.D. Nikolić, Influence of the exchange current density and overpotential for hydrogen evolution reaction on the shape of electrolytically produced disperse forms, J. Electrochem. Sci. Eng. 10 (2) (2020) 111–126.
[54] B. Seger, I.E. Castelli, P.C. Vesborg, K.W. Jacobsen, O. Hansen, I. Chorkendorff, 2-Photon tandem device for water splitting: comparing photocathode first versus photoanode first designs, Energy Environ. Sci. 7 (8) (2014) 2397–2413.
[55] B. Parkinson, On the efficiency and stability of photoelectrochemical devices, Acc. Chem. Res. 17 (12) (1984) 431–437.
[56] N. Papageorgiou, Counter-electrode function in nanocrystalline photoelectrochemical cell configurations, Coord. Chem. Rev. 248 (13–14) (2004) 1421–1446.
[57] D.C. Bookbinder, N.S. Lewis, M.G. Bradley, A.B. Bocarsly, M.S. Wrighton, Photoelectrochemical reduction of N, N′-dimethyl-4,4′-bipyridinium in aqueous media at p-type silicon: sustained photogeneration of a species capable of evolving hydrogen, J. Am. Chem. Soc. 101 (26) (1979) 7721–7723.
[58] Q. Chen, G. Fan, H. Fu, Z. Li, Z. Zou, Tandem photoelectrochemical cells for solar water splitting, Adv. Phys. X 3 (1) (2018) 1487267.
[59] X. Zhang, A. Bieberle-Hütter, Modeling and simulations in photoelectrochemical water oxidation: from single level to multiscale modeling, ChemSusChem 9 (11) (2016) 1223–1242.
[60] J. Yang, D. Wang, H. Han, C. Li, Roles of cocatalysts in photocatalysis and photoelectrocatalysis, Acc. Chem. Res. 46 (8) (2013) 1900–1909.
[61] L. Zhang, High-power energy storage: ultracapacitors, in: Modeling, Dynamics and Control of Electrified Vehicles, Elsevier, 2018, pp. 39–75.
[62] D. Noren, M.A. Hoffman, Clarifying the Butler–Volmer equation and related approximations for calculating activation losses in solid oxide fuel cell models, J. Power Sources 152 (2005) 175–181.
[63] D. Vikraman, S. Hussain, K. Karuppasamy, A. Feroze, A. Kathalingam, A. Sanmugam, S.-H. Chun, J. Jung, H.-S. Kim, Engineering the novel $MoSe_2$-Mo_2C hybrid nanoarray electrodes for energy storage and water splitting applications, Appl. Catal. B, Environ. 264 (2020) 118531.
[64] S.K. Murthy, A.K. Sharma, C. Choo, E. Birgersson, Analysis of concentration overpotential in an all-vanadium redox flow battery, J. Electrochem. Soc. 165 (9) (2018) A1746.
[65] R. Suwanwarangkul, E. Croiset, M. Fowler, P. Douglas, E. Entchev, M. Douglas, Performance comparison of Fick's, dusty-gas and Stefan–Maxwell models to predict the concentration overpotential of a SOFC anode, J. Power Sources 122 (1) (2003) 9–18.
[66] C. Gabrielli, F. Huet, R. Nogueira, Fluctuations of concentration overpotential generated at gas-evolving electrodes, Electrochim. Acta 50 (18) (2005) 3726–3736.
[67] S. Niu, S. Li, Y. Du, X. Han, P. Xu, How to reliably report the overpotential of an electrocatalyst, ACS Energy Lett. 5 (4) (2020) 1083–1087.
[68] J.R. Bolton, A.F. Haught, R.T. Ross, Photochemical energy storage: an analysis of limits, in: Photochemical Conversion and Storage of Solar Energy, 1981, pp. 297–330.
[69] J.A. Nelson, The Physics of Solar Cells, World Scientific Publishing Company, 2003.
[70] T.J. Jacobsson, V. Fjällström, M. Edoff, T. Edvinsson, A theoretical analysis of optical absorption limits and performance of tandem devices and series interconnected architectures for solar hydrogen production, Sol. Energy Mater. Sol. Cells 138 (2015) 86–95.
[71] M.A. El-Sayed, Triplet state. Its radiative and nonradiative properties, Acc. Chem. Res. 1 (1) (1968) 8–16.
[72] G. Committee, et al., Tables for reference solar spectral irradiances: direct normal and hemispherical on 37 tilted surface, ASTM International, 2012.
[73] J.H. Kim, D. Hansora, P. Sharma, J.-W. Jang, J.S. Lee, Toward practical solar hydrogen production–an artificial photosynthetic leaf-to-farm challenge, Chem. Soc. Rev. 48 (7) (2019) 1908–1971.
[74] H. Wendt, E.V. Spinacé, A. Oliveira Neto, M. Linardi, Electrocatalysis and electrocatalysts for low temperature fuel cells: fundamentals, state of the art, research and development, Quím. Nova 28 (6) (2005) 1066–1075.
[75] C. Song, J. Zhang, Electrocatalytic oxygen reduction reaction, in: PEM Fuel Cell Electrocatalysts and Catalyst Layers, Springer, 2008, pp. 89–134.
[76] R. Chen, S. Zamulko, D. Huang, C. Persson, Theoretical analyses of copper-based solar cell materials for the next generation of photovoltaics, CHAPTER 5, in: Solar Energy Capture Materials, The Royal Society of Chemistry, 2019, pp. 193–240, 08 2019.
[77] A.B. Murphy, P.R. Barnes, L.K. Randeniya, I.C. Plumb, I.E. Grey, M.D. Horne, J.A. Glasscock, Efficiency of solar water splitting using semiconductor electrodes, Int. J. Hydrog. Energy 31 (14) (2006) 1999–2017.